Boosting Photoelectrochemical Water Oxidation of Hematite in Acidic Electrolytes by Surface State Modification

Peng-Yi Tang, Li-Juan Han, Franziska Simone Hegner, Paul Paciok, Martí Biset-Peiró, Hong-Chu Du, Xian-Kui Wei, Lei Jin, Hai-Bing Xie, Qin Shi, Teresa Andreu, Mónica Lira-Cantú, Marc Heggen, Rafal E. Dunin-Borkowski, Núria López, José Ramón Galán-Mascarós, Joan Ramon Morante,* and Jordi Arbiol*

State-of-the-art water-oxidation catalysts (WOCs) in acidic electrolytes usually contain expensive noble metals such as ruthenium and iridium. However, they too expensive to be implemented broadly in semiconductor photoanodes for photoelectrochemical (PEC) water splitting devices. Here, an Earth-abundant CoFe Prussian blue analogue (CoFe-PBA) is incorporated with core–shell Fe_2O_3/Fe_2TiO_5 type II heterojunction nanowires as composite photoanodes for PEC water splitting. Those deliver a high photocurrent of 1.25 mA cm^{-2} at 1.23 V versus reversible reference electrode in acidic electrolytes (pH = 1). The enhancement arises from the synergic behavior between the successive decoration of the hematite surface with nanolayers of Fe_2TiO_5 and then, CoFe-PBA. The underlying physical mechanism of performance enhancement through formation of the $Fe_2O_3/Fe_2TiO_5/$ CoFe-PBA heterostructure reveals that the surface states' electronic levels of hematite are modified such that an interfacial charge transfer becomes kinetically favorable. These findings open new pathways for the future design of cheap and efficient hematite-based photoanodes in acidic electrolytes.

1. Introduction

Photoelectrochemical (PEC) water splitting devices, using Earth-abundant semiconductor materials, have long been considered to be the "Holy Grail" of solar energy conversion.[1–9]

For the design of a beneficial device structure, in which both electrodes are exposed to the same medium, and considering that the hydrogen evolution is most efficiently carried out in acidic electrolyte and the advantages of the proton exchange membrane, a robust photoanode would be highly desirable.[10–15] Nonetheless the development of an efficient and affordable photoanode, which is stable in acidic electrolyte, imposes a great challenge and limits the large-scale implementation of economically viable PEC water-splitting. In light of this challenge, much attention has been drawn to the development of efficient and affordable photoanode systems adapted to acidic electrolytes.

Hematite is arguably the most desirable photoanode material. On one hand, its relatively small bandgap of 1.9-2.1 eV and its suitably aligned valence band level perfectly match the thermodynamic energy requirements needed to drive water oxidation.[4,10] On the other hand, it is made from the most abundant transition metal on Earth crust, iron. Unfortunately, the bare hematite surface is catalytically very poor, and therefore requires modification with water-oxidation catalysts (WOCs) in order to extract the thermodynamic power stored when light is absorbed.

Dr. P.-Y. Tang, Dr. H.-B. Xie, Dr. M. Lira-Cantú, Prof. J. Arbiol
Catalan Institute of Nanoscience and Nanotechnology (ICN2)
CSIC and BIST
Campus UAB
Bellaterra 08193, Barcelona, Catalonia, Spain
E-mail: arbiol@icrea.cat
Dr. P.-Y. Tang, M. Biset-Peiró, Dr. Q. Shi, Dr. T. Andreu
Prof. J. R. Morante
Catalonia Institute for Energy Research (IREC)
Jardins de les Dones de Negre 1, Sant Adrià del Besòs,
Barcelona 08930, Catalonia, Spain
E-mail: jrmorante@irec.cat

The ORCID identification number(s) for the author(s) of this article can be found under https://doi.org/10.1002/aenm.201901836.

Dr. L.-J. Han, Dr. F. S. Hegner, Prof. N. López, Prof. J. R. Galán-Mascarós
Institute of Chemical Research of Catalonia (ICIQ)
BIST
Avinguda Països Catalans 16, Tarragona 43007, Catalonia, Spain
Dr. P.-Y. Tang, Dr. P. Paciok, Dr. H.-C. Du, Dr. X.-K. Wei, Dr. L. Jin,
Dr. M. Heggen, Prof. R. E. Dunin-Borkowski
Ernst Ruska-Centre for Microscopy and Spectroscopy with Electrons
and Peter Grünberg Institute
Forschungszentrum Jülich GmbH
52425 Jülich, Germany
Prof. J. R. Galán-Mascarós, Prof. J. Arbiol
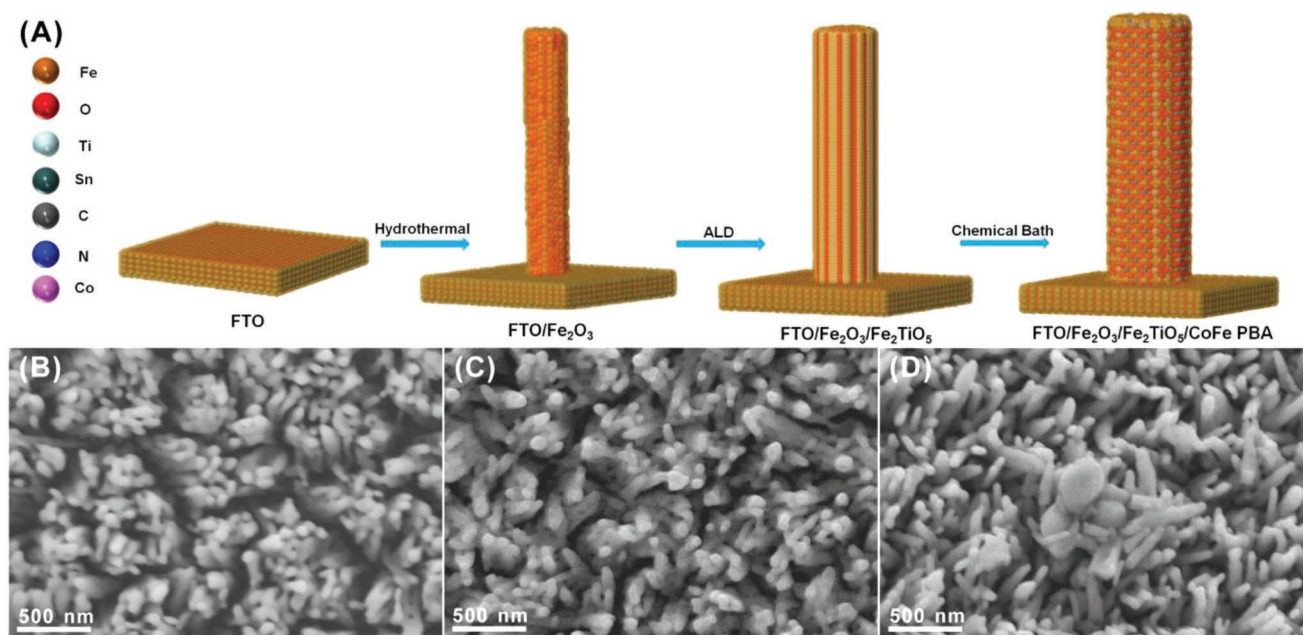ICREA
Pg. Lluís Companys 23, 08010 Barcelona, Catalonia, Spain

Figure 1. A) 3D Atomic supercell models with solvent accessible surface illustrating the synthetic procedure for Fe_2O_3/Fe_2TiO_5/CoFe PBA photoanodes. SEM images of B) Fe_2O_3, C) Fe_2O_3/Fe_2TiO_5, and D) Fe_2O_3/Fe_2TiO_5/CoFe PBA electrodes.

Regarding efficient WOCs in acidic electrolyte, many researchers have hitherto devoted their efforts to explore cheap, effective alternatives to the state-of-the-art ruthenium (Ru)- and iridium (Ir)-based WOCs.[14–18] For example, cobalt-containing polyoxometalates,[16] Ti-stabilized MnO_2,[19] $W_{1-x}Ir_xO_{3-\delta}$,[20] $Ni_xMn_{1-x}Sb_{1.6-1.8}O_y$,[21] Fe-TiO$_x$,[22] iron (III) oxide,[23] cobalt-doped hematite,[24] and CoFe-PBA[25,26] WOCs have been substantially explored. For a successful WOC-functionalized photoanode, it is necessary to consider the utilization of light capture of semiconductors and the catalytic effect of WOCs simultaneously, that is to say, boosting the performance of the WOCs without compromising the light absorption features.[11,12] Up to date, few reports have appeared on smart integration of hematite with WOCs, and most of them related to noble Ir-based catalysts,[11,27–29] with which a maximum photocurrent response of 0.66 mA cm^{-2} at 1.23 V versus reversible reference electrode (RHE) in acidic electrolyte (pH = 1.01) was obtained.[11] Thus, even by coupling with noble Ir-based WOCs, the photocurrent response of hematite based photoanodes in acidic electrolyte remains much lower than its theoretical value (12.5 mA cm^{-2}).[30]

Meanwhile, it is well established that the surface states present in the bandgap of hematite, mediate hole transfer and plays a vital role in determining its PEC performance.[31,32] There are two types of surface states, intrinsic surface states derived from the loss of translational bulk crystal symmetry, and extrinsic surface states due to chemical bond formation/surface interaction with a secondary species.[33,34] While it is difficult to completely remove intrinsic surface states, they can be modified by depositing a secondary species,[35] which has recently been demonstrated.[28,36–38] For instance, our previous investigation about ITO/Fe_2O_3/Fe_2TiO_5/FeNiOOH photoanodes in alkaline electrolytes reveals that the surface states of hematite

can be modified by atomic layer–deposited Fe_2TiO_5 and photoelectrodeposited FeNiOOH.[38] Moreover, hematite photoanodes were combined with a CoFe-PBA resulting in enhanced photocurrent response in neutral electrolyte.[37] Despite these observations in neutral and alkaline electrolytes, rare reports on the performance of hematite-based photoanodes in acidic media have been published, despite the extraordinary technological interest, as described above.

With the aim of designing cheap and efficient hematite-based photoanodes in acidic electrolyte, we decided to merge these two previous strategies. First, we fabricated core–shell Fe_2O_3/Fe_2TiO_5 type II heterostructured nanowires, as a surface-modification approach to enhance photocatalytic activity. Second, we decorated these nanowires with a nanolayer of an acid-stable WOC, the CoFe-PBA (Scheme S1, Supporting Information). These photoanodes were prepared on fluoride-doped tin oxide (FTO) glass electrodes in three steps: hydrothermal deposition of Fe_2O_3; atomic layer deposition (ALD) of Fe_2TiO_5; and finally, chemical bath deposition of CoFe-PBA, as displayed in **Figure 1**A. These heterostructures are able to produce the highest photocurrent response in acid media ever observed for a hematite-based photoanode, when made by scalable processes, and earth-abundant materials, opening new strategies for hematite-based PEC water splitting in acidic electrolyte.

2. Results and Discussion

2.1. Processing and Structural Characterization

Vertically aligned Fe_2O_3 nanowires with diameters ranging from 100 to 200 nm (Figure 1B) were first grown on a FTO substrate via a hydrothermal method.[38] Then, a thin TiO_2

layer was coated onto the Fe_2O_3 nanowires by 30 ALD cycles. The surface coated TiO_2 was subsequently transformed into Fe_2TiO_5 through a post-sintering process in ambient atmosphere at 750 °C for 30 min. As displayed in Figure 1C, the Fe_2O_3/Fe_2TiO_5 heterostructured nanowires are homogeneous without changing the nanowire-like architecture. Subsequently, the obtained Fe_2O_3/Fe_2TiO_5 composite nanowires were subjected to a chemical bath for 2 h in the presence of the CoFe-PBA precursor at 60 °C to produce $Fe_2O_3/Fe_2TiO_5/CoFe$-PBA heterostructured nanowires. Its scanning electron microscope (SEM) image in Figure 1D reveals that the diameter of these nanowires did not change compared to the Fe_2O_3/Fe_2TiO_5 ones, indicating the ultrathin CoFe-PBA coating. The sample crystallinity and chemical composition were further analyzed via energy dispersive X-ray spectroscopy (EDX), X-ray photoelectron spectroscopy (XPS), and X-ray diffraction (XRD), Raman spectrum, and Fourier transform infrared (FT-IR) spectrum in Figures S1-S5 in the Supporting Information, evidencing the existence of hematite, Fe_2TiO_5, and CoFe-PBA species in the corresponding electrodes.

The structure, crystallography, and spatial distribution of hematite, Fe_2TiO_5, and CoFe-PBA species were further investigated by aberration-corrected scanning transmission electron microscopy (AC-STEM) in high angle annular dark-field (HAADF) mode. On one hand, the HAADF STEM images of Fe_2O_3 and Fe_2O_3/Fe_2TiO_5 electrodes on the top and middle rows of **Figure 2** show the atomic ordering of the hematite matrix. On the other hand, the Fe_2TiO_5 species in the Fe_2O_3/Fe_2TiO_5 electrode are shown as a blurred ultrathin shell on the surface of the hematite nanowires (middle rows of Figure 2 and Figure S10, Supporting Information), in good agreement with the maps obtained by STEM combined with electron energy loss spectroscopy (EELS) in Figure S12 in the Supporting Information conducted on the same region. The additional atomic resolution HAADF STEM imaging in combination with the STEM-EELS compositional maps of the Fe_2O_3 and Fe_2O_3/Fe_2TiO_5 electrodes are included in Figures S6–S12 in the Supporting Information, confirming the core–shell nanowires structure of the Fe_2O_3/Fe_2TiO_5 electrode. Notably, coordination polymers are especially susceptible to the electron beam damage, hindering stable atomic-level HAADF STEM observation of the CoFe-PBA.[25,38–41] Thus, we employed bright field HRTEM to monitor the surface structure evolution of the $Fe_2O_3/Fe_2TiO_5/CoFe$-PBA electrodes.

Figure 2A displays a representative TEM image of a $Fe_2O_3/Fe_2TiO_5/CoFe$-PBA nanowire. According to Figure 2B-D, the nanoparticles attached to the composite nanowire can be assigned to CoFe-PBA species. The hematite and Fe_2TiO_5 phases dominate the nanowires matrix, as identified by the HRTEM and its corresponding power spectrum in Figure 2E-F. Moreover, the corresponding frequency filtered image (Figure 2G) clearly illustrates the presence of a localized hematite nanowire core and an ultrathin pseudo-brookite shell. Figure 2E and Figure S13 in the Supporting Information show that the fine CoFe-PBA shell on the nanowires surface tends to possess an amorphous structure, whereas bigger CoFe-PBA nanoparticles present lattice fringes denoting its good crystallinity, as displayed in Figure 2C and Figure S14 in the Supporting Information.

The spatial elemental distribution of $Fe_2O_3/Fe_2TiO_5/CoFe$-PBA electrodes was further characterized via HAADF STEM combined with EELS. In addition to the elemental signals from the CoFe-PBA nanoparticles, we also found the presence of C, N, O, Co, and Fe surrounding the nanowire matrix in the STEM-EELS maps shown in **Figure 3** and Figures S15-S16 in the Supporting Information.[25] These results evidence that the surface amorphous region observed in Figure 2E is indeed an ultrathin CoFe-PBA shell at the surface of the Fe_2O_3/Fe_2TiO_5 nanowires. Additionally, the statistical diameter size distributions of Fe_2O_3, Fe_2O_3/Fe_2TiO_5, and $Fe_2O_3/Fe_2TiO_5/CoFe$ PBA nanowires in Figure S17 in the Supporting Information reveal that Fe_2O_3, Fe_2O_3/Fe_2TiO_5, $Fe_2O_3/Fe_2TiO_5/CoFe$ PBA nanowires have average diameter size of 168 ± 43, 174 ± 63, and 185 ± 70 nm, respectively. The average diameter size of these nanowires did not significantly change with the coating of Fe_2TiO_5 and CoFe PBA, which is consistent with the SEM results.

2.2. Photoelectrochemical Performance

The detailed PEC performance measured for these photoanodes is displayed in **Figure 4**. Cyclic voltammtry (CV) measurements in the dark (Figure 4A) show a positive shift of the onset potential of hematite upon coating with the ultrathin Fe_2TiO_5 shell, consistent with our previous work,[38] whereas modification with CoFe-PBA reduces the onset potential of the Fe_2O_3/Fe_2TiO_5 electrode, which demonstrates the positive catalytic effect of CoFe-PBA. Under light irradiation, the CV in Figure 4B and the statistical data in Figure S18 in the Supporting Information reveal that pristine Fe_2O_3 electrodes exhibit a very low photocurrent response of 0.12 mA cm^{-2} at 1.23 V versus RHE, the thermodynamic potential for the oxygen evolution reaction.[42] Upon Fe_2TiO_5 deposition, the photocurrent density increases significantly above 1.0 V versus RHE, reaching 0.90 mA cm^{-2} at 1.23 V versus RHE (Figure 4B). The onset potential is further improved for the $Fe_2O_3/Fe_2TiO_5/CoFe$-PBA electrode. This parameter was used to optimize the $Fe_2O_3/Fe_2TiO_5/CoFe$-PBA processing (Figures S19-S20, Supporting Information). According to the statistical data in Figure S19 in the Supporting Information, we reached a maximum PEC performance with electrodes coated with CoFe-PBA by a chemical bath reaction at 60 °C for 2 h, giving 1.25 mA cm^{-2} at 1.23 V versus RHE. To the best of our knowledge, this is the highest photocurrent value observed for hematite-based photoanodes in acidic electrolyte (see Table S1, Supporting Information). Moreover, it is better than the photocurrent response for Fe_2O_3/Fe_2TiO_5 (0.90 mA cm^{-2}, Figure 4B) and $Fe_2O_3/CoFe$-PBA (0.62 mA cm^{-2}, based on the statistical data in Figures S21-S22, Supporting Information) electrodes indicating a synergic effect in combining core–shell Fe_2O_3/Fe_2TiO_5 type II heterojunction with the CoFe-PBA WOC.

The chopped light photocurrent–potential curves in Figure 4C show smaller photocurrent transients for the $Fe_2O_3/Fe_2TiO_5/CoFe$-PBA electrodes, in particular in the potential range of 1.2–1.7 V versus RHE. This reduction of the photocurrent transient indicates that the electron–hole recombination is suppressed by the Fe_2TiO_5 and CoFe-PBA modification, further demonstrating
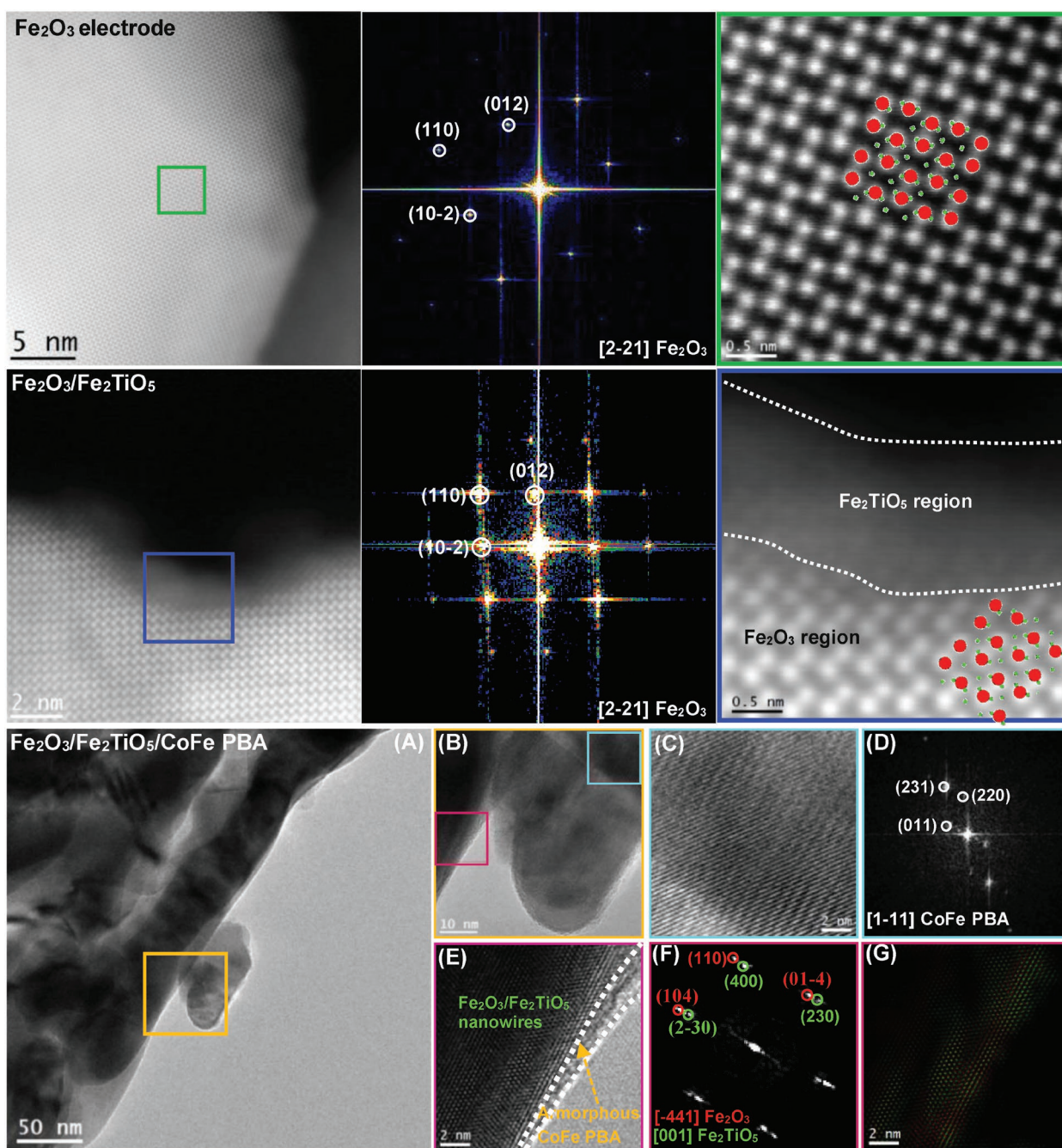
Figure 2. Top row: (Left) HAADF STEM image showing the atomic ordering at the edge region of the Fe_2O_3 electrode. (Middle) the corresponding colored fast Fourier transform power spectrum (FFT) indicates that the nanowires crystallize in the hematite phase as visualized along the [2–21] direction. (Right) Atomic resolution HAADF STEM image of the green squared region showing the ordering of Fe, while O atoms are almost not visible in HAADF STEM mode due to the their weak Z-contrast. Middle row: (Left) HAADF STEM image showing the atomic ordering at the edge region of the Fe_2O_3/Fe_2TiO_5 electrode. (Middle) The corresponding colored FFT spectrum indicates that the nanowires matrix is hematite as visualized along the [2–21] direction. (Right) Atomic resolution HAADF STEM image of the blue squared region showing the typical ordering of Fe atoms in hematite. The Fe_2TiO_5 shell is observed as a blurred ultrathin shell ($\approx$1 nm) on the surface of the hematite matrix since the heights of hematite-core and Fe_2TiO_5 shell are different. (the inset shows the atomic model of Fe and O atoms visualized from the [2–21] direction, with Fe atoms marked as red and O atoms marked as green). Bottom row: A) low magnification bright field TEM images showing the general morphology of the $Fe_2O_3/Fe_2TiO_5/CoFe$-PBA nanowires. B) HRTEM detail showing the yellow squared interface area in (A). C) Magnified HRTEM detail of the selected surface nanoparticle and D) corresponding power spectrum indicating that the nanoparticle attached to the nanowire matrix crystallized in the cubic CoFe-PBA phase, as visualized along the [1–11] direction. E) HRTEM image of the nanowire surface region squared in purple in (B). The white dotted line is marking an amorphous CoFe-PBA region. F) Corresponding FFT spectrum indicating that the nanowire heterostructure is mainly composed of hematite and pseudobrookite as visualized along the [–441] and [001] directions, respectively. G) Frequency filtered structural map of the hematite (red) and pseudobrookite (green), showing their atomic stack sequence.
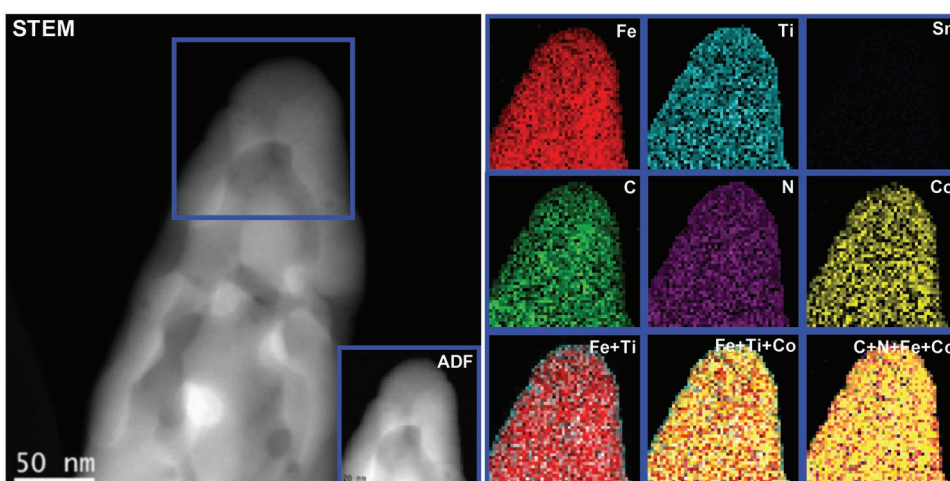
Figure 3. High magnification EELS chemical composition maps obtained from the blue rectangle area in the ADF-STEM micrograph of a nanowire extracted from the Fe$_2$O$_3$/Fe$_2$TiO$_5$/CoFe-PBA electrode. Individual Fe (red), C (green), Sn (blue), N (purple), Ti (indigo), and Co (yellow) maps and their composites.

its advantage. Moreover, the UV–vis absorptance, Tauc plots, IPCE, and APCE spectra of the Fe$_2$O$_3$, Fe$_2$O$_3$/Fe$_2$TiO$_5$, and Fe$_2$O$_3$/Fe$_2$TiO$_5$/CoFe PBA electrodes in Figure S23 in the Supporting Information further evidence that the enhanced PEC performance of Fe$_2$O$_3$/Fe$_2$TiO$_5$/CoFe-PBA electrodes is attributed to the synergetic effect from Fe$_2$TiO$_5$ and CoFe-PBA.

The PEC stability of these three electrodes was investigated by chronoamperometry at a constant applied working potential of 1.23 V versus RHE (Figure 4D) at pH = 1 for 24 h. The photocurrent response of Fe$_2$O$_3$ electrodes shows a slow but continuous decrease, maintaining about 40% of the initial photocurrent response after 24 h test. In contrast, Fe$_2$O$_3$/Fe$_2$TiO$_5$ and Fe$_2$O$_3$/Fe$_2$TiO$_5$/CoFe-PBA electrodes follow a similar trend, showing an initial drop in photocurrent during the first 2 h and show no further sign of fatigue during the rest of the stability measurement, retaining around 80% of the initial photocurrent response after 24 h test. Additionally, we monitored the evolved oxygen in the case of Fe$_2$O$_3$/Fe$_2$TiO$_5$/CoFe-PBA electrodes by a calibrated Fibox O$_2$ detector in a gastight cell during the first 2 h water oxidation at 1.23 V versus RHE (Figure S24A, Supporting Information). The theoretical oxygen yield was calculated from the total charge passed during PEC water oxidation. Faradaic Efficiencies above 94% were demonstrated (Figure S24B, Supporting Information), indicating that the photocurrent response is mainly originating from the water oxidation process. The enhanced stability of Fe$_2$O$_3$/Fe$_2$TiO$_5$ and Fe$_2$O$_3$/Fe$_2$TiO$_5$/CoFe-PBA electrodes compared to Fe$_2$O$_3$ electrodes is further confirmed by the CV curves of these electrodes after 24 h stability test in Figure S25 in the Supporting Information. Moreover, the SEM images of Fe$_2$O$_3$ electrodes after 24 h stability measurement in Figure S26A-C in the Supporting Information reveal that the attenuation of the photocurrent response in Fe$_2$O$_3$ electrodes is derived from its nanowires structure degradation in acidic electrolyte. In contrast, the degradation of Fe$_2$O$_3$/Fe$_2$TiO$_5$, and Fe$_2$O$_3$/Fe$_2$TiO$_5$/CoFe-PBA electrodes' nanowires are substantially suppressed, as displayed in Figure S26D-I in the Supporting Information. Therefore, we assign the drastically enhanced stability of Fe$_2$O$_3$/Fe$_2$TiO$_5$/CoFe-PBA electrodes to the dual protective effect provided by the Fe$_2$TiO$_5$ and the CoFe-PBA (Figure 4E), both of which are stable in acidic electrolytes. [19,22,25,43]

2.3. Mechanistic Investigation via Photoelectrochemical Impedance Spectroscopy (PEIS)

It is well established that the catalytic activity of photoanodes is strongly dependent on the characteristics of the surface states at the semiconductor-electrolyte interface (SEI).[44–46] While those surface states can limit water oxidation kinetics by acting as electron–hole recombination centers, they can also have a beneficial influence on water oxidation, promoting electron transfer across the interface, dependent on their respective kinetics.[47] In particular, electrical active surface states presented in the hematite bandgap are supposed to play a vital role in PEC water oxidation; thus, a deeper investigation is required to probe their effect on charge transfer at the SEI (Figure 4E).[38,48–51]

We employed CV and PEIS techniques to monitor the evolution of such surface states in hematite,[44,45] which was suggested to be an iron-oxo intermediate by operando IR spectroscopy[48] and density functional theory calculations[52,53] and how it is influenced by successive Fe$_2$TiO$_5$ and CoFe-PBA deposition. As displayed in **Figure 5**A, the precatalytic feature in the CV, which is related to adding and removing electrons to/from the surface states, changes with the addition of Fe$_2$TiO$_5$ and CoFe-PBA.[48] Their significant impact on the surface states was further suggested by PEIS. The equivalent circuits in Figure S29 in the Supporting Information were used to fit the obtained data in Figures S27-S28 in the Supporting Information; the obtained resistances and capacitances are shown in Figures S30-S31 in the Supporting Information.

From the fitted surface states or trap capacitance C_{trap}, we estimated the density of surface states (DOSS) with Equation (1)[32,36,54,55]

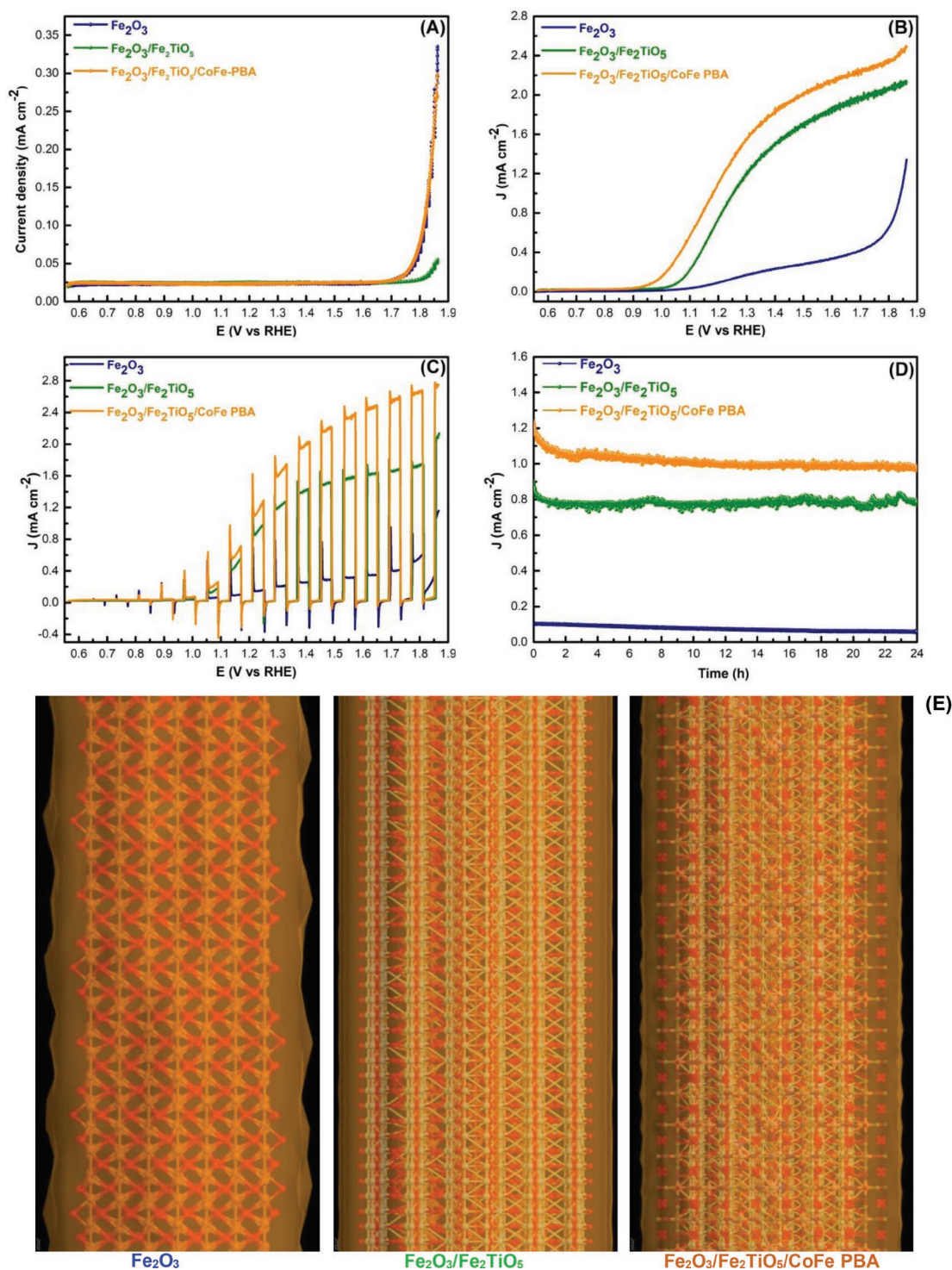$$N_{SS}(E) = \frac{C_{trap}(E)}{q} \tag{1}$$

Figure 4. A) Cyclic voltammetry under dark, B) cyclic voltammetry under illumination, C) chopped light photocurrent–potential curves, and D) photo-electrochemical stability test operated at 1.23 V versus RHE of the Fe_2O_3, Fe_2O_3/Fe_2TiO_5, and $Fe_2O_3/Fe_2TiO_5/CoFe$-PBA electrodes for 24 h. All polarization potentials reported here are relative to the RHE, and current densities are based on the geometric area. J (mA cm^{-2}) represents the current density response under light illumination. E) Zoom in view of the atomic supercell model with solvent accessible surface of Fe_2O_3, Fe_2O_3/Fe_2TiO_5, and $Fe_2O_3/Fe_2TiO_5/CoFe$-PBA nanowires show the modified surface interfaces.

where N_{ss} (E) is the DOSS (cm^{-2} eV^{-1}) as a function of the applied potential and q is the electron charge (1.602×10^{-19} C). As shown in Figure 5B, the energy and density distribution of the surface states N_{ss}[32,54] follows the order Fe_2O_3 < $Fe_2O_3/$ Fe_2TiO_5 < $Fe_2O_3/Fe_2TiO_5/CoFe$-PBA across the entire surface states dominated region (0.86 to 1.46 V). The extended
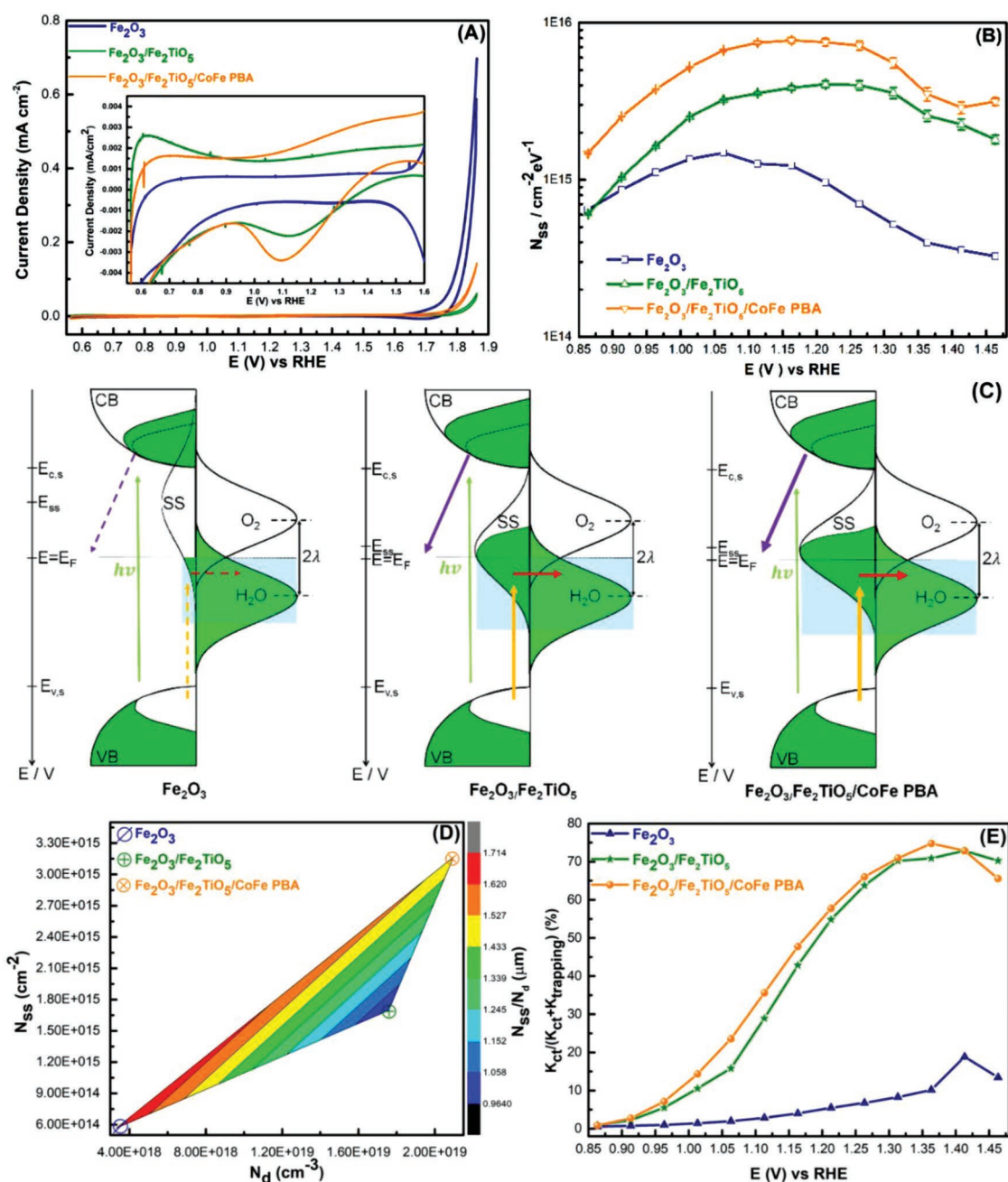
Figure 5. A) CV curves scanned immediately in dark at 20 mV s⁻¹ after holding the electrode potential at 1.85 V versus RHE for 1 min under illumination (the inset shows its magnified plot). B) DOSS as a function of the applied potential. Error bars stem from the goodness of the EIS data fittings. C) Kinetic scheme of the charge generation and transfer processes at the SEI at 1.23 V versus RHE under illumination of these electrodes. Green and white areas represent electron filled and empty states, respectively. The dotted lines marked region in the CB filled states refer to photogenerated electrons with the same relative area as the empty states at the VB; the exceeding green regions highlight the doping levels in these electrodes. The green arrows denote the charge generation process upon photons absorption; the yellow arrows denote the hole trapping process at SS (surface states); the red arrows denote the hole transfer process from the SS to the electrolyte; the purple arrows denote electron transfer from CB states to the FTO substrates. The thickness and shape of the arrows reveal the relative rates of the charge transfer processes, where the dotted lines mean the slowest rate (Fe₂O₃ electrode) and the thickest lines means the fastest rate (Fe₂O₃/Fe₂TiO₅/CoFe-PBA electrode). The light indigo shaded areas refer to the relative overlapping of the DOSS and water density of states. E: electrode potential; $E_{c,s}$: surface CB edge potential; E_F: Fermi level of the semiconductors that matches the electrode potential E) and the O₂/H₂O couple's thermodynamic potential (1.23 V vs RHE); E_{SS}: center potential of the SS distribution; $E_{v,s}$: surface VB edge potential; λ: redox couple reorganization energy. It is worth noting that the relative size of the DOSS distribution for these electrodes has been intentionally enlarged to highlight the SS. D): Total surface state density (N_{ss}), donor density (N_d), and their ratio (N_{ss}/N_d) plot. N_d was estimated from the slopes of the Mott–Schottky plots (Figure S30, Supporting Information), whereas N_{ss} was obtained from integration of the DOSS profiles. Color bar with a unit of µm is plotted at the right Y axis for N_{ss}/N_d. E) Ratio of the charge transfer rate constant (k_{ct}) and the sum of k_{ct} and trapping rate constant ($k_{trapping}$) at different potentials.

surface states distribution from 0.86 to 1.46 V in unmodified Fe_2O_3 electrodes probably spans inside the CB, where recombination with CB electrons may occur. Moreover, it triggers a deleterious Fermi level pinning, which also contributes to its low photocurrent response.[54] Upon surface modification, the DOSS maximum shifts to more positive potentials, i.e., further into the bandgap, which minimizes overlap with the conduction band (Figure 5C). Further, its shape coincides well with the cathodic CV curves obtained after holding the electrodes at a potential of 1.85 V versus RHE for 1 min (Figure 5A), which also indicates the correct utilization of the equivalent circuit model for PEIS fitting.[44,48] Consequently, the ultrathin Fe_2TiO_5 and CoFe-PBA coatings indeed work together modifying the density and energy level of the surface states in hematite photoanodes.

Assuming surface states mediated charge-transfer (CT), the CT rate constant (k_{ct}) at a certain electrode polarization potential (E), is proportional to Equation (2)[28,32,54-56]

$$k_{ct} \propto \int_{E_{v,s}}^{E} N_{ss} f(E) D_{H_2O}(E) dE \qquad (2)$$

in which $f(E)$ is the Fermi–Dirac distribution indicating the fraction of occupied surface states and $D_{H_2O}(E)$ is the water density of states (cm^{-2} eV^{-1}). Given that the inelastic hole trapping process mediated by surface states is fast enough,[53] the photocurrent response is proportional to k_{ct},[57] depending on the overlap between the filled surface states and the filled water density of states. There is, thus, a direct correlation between the percentage of available filled surface states (larger DOSS) near the thermodynamic potential for water oxidation and the observed photocurrent response at 1.23 V versus RHE because of the required isoenergetic hole transfer process at the SEI.[38,54,55] As illustrated in Figure 5C, the $Fe_2O_3/Fe_2TiO_5/$CoFe-PBA electrode possesses the highest photocurrent response at 1.23 V versus RHE due to the maximum energy level matching between the surface states of the photoanodes and the water density of states.

Furthermore, a combined comparison of the N_{ss}, N_d, and N_{ss}/N_d ratio is presented in Figure 5D. The pristine Fe_2O_3 electrodes present a relatively high N_{ss}/N_d ratio but poor PEC performance, indicating that a large N_{ss}/N_d ratio does not guarantee a good photocurrent response due to the lack of donors and low electrical conductivity. For the Fe_2O_3/Fe_2TiO_5 electrodes, the N_d is promoted via Ti doping, and this enables a higher photocurrent. In the case of the $Fe_2O_3/Fe_2TiO_5/$CoFe-PBA electrode, N_{ss} and N_d are both numerous enough to further increase the photocurrent response.

The charge transfer efficiency at the SEI is first estimated by Equation (3)[33,54,57,58]

$$\text{Transfer efficiency } (\%) = \frac{k_{ct}}{k_{ct} + k_{trapping}} = \frac{R_{trapping}}{R_{ct,trap} + R_{trapping}} \qquad (3)$$

where k_{ct} and $k_{trapping}$ are the charge transfer and trapping rate constants, respectively, and R_{ct} and $R_{trapping}$ are the corresponding resistances. The calculated charge transfer efficiency from PEIS is shown in Figure 5E. In the case of the $Fe_2O_3/Fe_2TiO_5/$CoFe-PBA electrode, over 60% of the holes are

transferred into the electrolyte at 1.23 V versus RHE, which is almost 10 times as high as for pristine Fe_2O_3. Additionally, the calculated charge transfer efficiency of these electrodes is in good agreement with the steady-state current-voltage relationship (Figure 4B) and the charge separation efficiencies (Figure S32, Supporting Information) of Fe_2O_3, Fe_2O_3/Fe_2TiO_5 and $Fe_2O_3/Fe_2TiO_5/$CoFe-PBA electrodes obtained via comparing the cyclic voltammetry measurements in electrolyte with and without a hole scavenger, further confirming the highest charge transfer efficiency of the $Fe_2O_3/Fe_2TiO_5/$CoFe-PBA electrodes.[32]

3. Conclusion

In summary, we have successfully integrated Fe_2O_3 nanowires with an ultrathin Fe_2TiO_5 heterojunction and CoFe-PBA decoration for enhanced PEC water splitting in acidic electrolyte (pH = 1). Thanks to the combination of core–shell $Fe_2O_3/$ Fe_2TiO_5 type II heterojunction nanowires and the catalytic function of CoFe-PBA, $Fe_2O_3/Fe_2TiO_5/$CoFe-PBA composite photoanodes are able to deliver 1.25 mA cm^{-2} photocurrent at 1.23 V versus RHE, almost one order of magnitude photocurrent increment in comparison to the pristine Fe_2O_3 nanowires. By a systematic electrochemical investigation, the enhanced PEC performance of the $Fe_2O_3/Fe_2TiO_5/$CoFe-PBA composite electrode can be attributed to the modified surface states density after successive coatings, as well as the enhanced donor density derived from inevitable Ti doping during the high temperature sintering.[38] This work suggests that simultaneously employing the synergy of core–shell Fe_2O_3/Fe_2TiO_5 type II heterojunction and CoFe-PBA WOCs could be an effective approach to improve the PEC performance of photoanodes in acidic electrolytes, bringing new promise toward effective solar-fuel generation.

4. Experimental Section

Chemicals and Materials: All chemical reagents were purchased from Sigma-Aldrich and used without further purification. All solutions were prepared with Milli-Q water (≈18.2 MΩ cm resistivity). FTO substrate (735167-1EA, 7Ω sq^{-1}) was purchased from Sigma-Aldrich and pre-cleaned before using as substrates.

FTO Pre-Clean Process: FTO substrates were cut into small pieces (area: 1 cm × 3 cm) and washed by sonicating in a (1:1:1) mixture of acetone (99.9%), isopropanol (99.9%), and water. After rinsing thoroughly with distilled water, the FTO substrates were washed in ethanol (Fluka, 99.8%) and then dried in air at 300 °C for 1 h (heating rate: 8.5 °C min^{-1}). Then, part of the FTO substrates (≈1 cm × 2 cm) was covered using a polymer tape (Kaptons Foil, VWR International). The uncoated part of the FTO was later employed as electric contact for the working electrodes in the photoelectrochemical cell.

Fe_2O_3 Electrodes: Hematite nanowires were prepared according to our previously published procedure.[38] Typically, a 200 mL Teflon-lined stainless-steel autoclave was filled with 60 mL aqueous mixture solution of 0.15 M ferric chloride ($FeCl_3$, 97%), 1 M sodium nitrate ($NaNO_3$, 99%) and 316 μL hydrochloric (HCl, wt 37%). 6 pieces of FTO substrates were put into the autoclave, which was sealed and heated at 95 °C for 4 h. A homogenous layer of iron oxyhydroxide (FeOOH) nanowires was grown onto the FTO substrate. After that, the FeOOH-coated FTO substrates were washed with deionized water to remove any residual salts, and subsequently pre-sintered in air at 550 °C (heating rate: 8.5 °C min^{-1})

for 2 h to convert FeOOH nanowires into hematite nanowires. To further reduce the surface defective sites and improve the crystallinity, the obtained hematite nanowires were post-sintered at 750 °C in air for additional 30 min and cooled down to the room temperature in 1 min.

Fe₂O₃/Fe₂TiO₅ Electrodes: The obtained hematite samples, after a pre-sintering process (550 °C for 2h), were further subjected to an ALD TiO₂ process. The ALD TiO₂ was performed in a R200 picosun atomic layer deposition system at 150 °C with TiCl₄ (99.9%) and water as the precursors in an 8 mbar N₂ flow atmosphere with a growth rate of 0.27 Å per cycle. The pulse time for the TiCl₄ and water were 0.1 s and the purge time was 10 s. The thickness of TiO₂ coating onto the Fe₂O₃ nanowires can be controlled by changing the ALD deposition cycle. In this case, the optimized TiO₂ layer corresponds to 30 cycles according to the previous report.[38] After that, a post-sintering process at 750 °C for 30 min was performed to transform the surface ALD TiO₂ into Fe₂TiO₅.[38,54]

Fe₂O₃/Fe₂TiO₅/CoFe-PBA Electrodes: The obtained Fe₂O₃/Fe₂TiO₅ electrodes were further coated with CoFe-PBA in a chemical bath.[25] Chemical bath deposition of CoFe-PBA on the Fe₂O₃/Fe₂TiO₅ electrodes were carried out according to the following procedure: First, Co(NO₃)₂₆H₂O (700 mg) and K₃Fe(CN)₆ (350 mg) powder were dissolved in 40 mL of Milli-Q water under vigorous stirring. After that, one piece of Fe₂O₃/Fe₂TiO₅ electrodes was immersed in a 5 mL glass vial with 4 mL freshly prepared mixture solution containing Co(NO₃)₂6H₂O + K₃Fe(CN)₆. The glass vial was sealed and then heated at 60 °C for different reaction times in the oven. Finally, the obtained samples were rinsed with Milli-Q water to remove any impurities and were dried in the oven at 60 °C overnight.

Structural and Morphological Characterization: The grazing incidence X-ray diffraction analyses were conducted on a Bruker D4 X-ray powder diffractometer via using the Cu Ka radiation (1.54184 Å) and a 1D Lynkeye detector, which was equipped with a Gobel mirror in the incident beam and equatorial Soller slits in the diffracted beam (51 incidence angle, 2° per step). The surface morphology of the electrodes was characterized via using a field emission gun scanning electron microscope (FE-SEM, Zeiss Series Auriga microscopy) equipped with an electron dispersive X-ray spectroscopy detector. X-ray photoelectron spectroscopy was performed with a Phoibos 150 analyser (SPECS GmbH, Berlin, Germany)) in an ultrahigh vacuum condition (base pressure 4×10^{-10} mbar) with a monochromatic aluminium K$_\alpha$ X-ray source (1486.74 eV). The energy resolution was 0.8 eV based on the FWHM measurement of the Ag 3d$_{5/2}$ peak for a sputtered silver foil. Infrared absorption spectroscopy was performed with a ThermoScientific NICOLET iS50 FT-IR spectrometer. Raman Spectrum was conducted at InVia-RENISHAW with incident wavelength: 514 nm. Optical properties of all electrodes were characterized by using a UV–vis spectrophotometer (Lambda 950, Perkin Elmer) equipped with an integrating sphere (150 mm diameter sphere covered with Spectralon as the reflecting material, Perkin Elmer). Absorbance (A) measurements were obtained from measured reflectance (R, %) and transmission (T, %), using a wavelength range from 350 to 800 nm and a step of 5 nm, respectively. All the samples for HRTEM and ADF-STEM were produced via using a mechanical process.[38] HRTEM and ADF-STEM images were obtained by using a FEI Tecnai F20 field emission gun microscope with a 0.19 nm point-to-point resolution at 200 kV equipped with an embedded Quantum Gatan image filter for EELS analyses. Atomic resolution AC HAADF STEM and further EELS-STEM analyses were conducted at a FEI TITAN 80–300 STEM operated at 300 kV and a TITAN G3 50–300 PICO operated at 80 kV.[59,60] Images were analyzed via using Gatan Digital Micrograph software. The Eje-Z, Rhodius, and JMOL software packages were employed for the atomic supercell modeling with the corresponding crystal phase parameters of each species obtained from the inorganic crystal structure database (ICSD).[61–63] Specifically, to further identify the crystal phases via HRTEM, HAADF STEM, and to probe the spatial distribution of these components in the composite hematite electrodes, we created crystal models based on the single crystal data found in the ICSD. With these crystal models, the diffraction patterns visualized from different zone axes of each species could be

simulated. Then, the simulated diffraction pattern was compared with the FFT spectrum obtained on the atomic resolution HRTEM and HAADF STEM experimental images for the identification of the crystal phases in the composite hematite electrodes.

Photo-Electrochemical Measurements: Photocurrent density (j, mA cm^{-2}) versus applied potential (E, V) curves were conducted using a three-electrode cell. The working, counter, and reference electrodes were the composite hematite photoanodes (1 cm² geometric area), a Pt wire, and an Ag/AgCl (3 M KCl) reference electrode (Metrohm, E = 0.203 versus NHE), respectively. The utilized electrolyte was a 0.1 M NaNO₃ + 0.1 M HNO₃ solution (pH = 1), which was purged with N₂ during the experiments. CV was taken using a computer-controlled potentiostat (VMP3, BioLogic Science Instruments). CV scan was from 0.30 V versus Ag/AgCl to 1.60 V versus Ag/AgCl, with a scan rate of 20 mV s^{-1}. The photocurrent density is calculated based on the geometric area. All potentials were corrected at 80% for the ohmic drop, which was determined using the automatic current interrupt (CI) method implemented by the potentiostat,[25] and were converted with respect to the RHE: E (V versus RHE) = E (V versus Ag/AgCl) + 0.0592 × pH + 0.203. Light illumination calibration was performed using a 150 W AM 1.5G solar simulator (Solar Light Co., 16S-300-002 v 4.0) with an incident light intensity set at 1 Sun illumination (100 mW cm^{-2}), as measured via using a thermopile (Gentec-EO, XLPF12-3S-H2-DO) coupled with an optical power meter (Gentec-EO UNO). In the PEC characterization, the light came from the front side (hematite-electrolyte interface, front side illumination). All the electrodes were repeated at least three times, and the statistical photocurrent response data at 1.23 V versus RHE are included in the Supporting Information.

Faradaic Efficiency Measurement: The O₂ generated under chronoamperometric conditions (1.23 V versus RHE) during 2 h and under 1 Sun illumination was measured with the calibrated Fibox detector immersed in the electrolyte in a gastight cell. The oxygen evolution efficiencies were determined from the total amount of charge Q (C) passed through the cell. Assuming that four holes are needed to produce one O₂ molecule, the theoretical yield can be calculated as follows:

$$n_{O_2} = \frac{Q}{4F} \tag{4}$$

where F is the Faraday constant. The total mole of oxygen produced was quantitatively determined by using a calibrated Fibox detector with a temperature sensor.

Incident Photon to Current Efficiency (IPCE): IPCE was characterized using a xenon light source (Abet 150 W Xenon Lamp) coupled with a monochromator (Oriel Cornerstone 260 1/4 m monochromator). The wavelength was scanned from 350 to 800 nm (step: 10 nm step^{-1}) keeping the voltage fixed at 1.23 V versus RHE. The IPCE was calculated based on the following equation[38]

$$IPCE(\%) = (1240/\lambda) \times (I/J_{light}) \times 100 \tag{5}$$

where I is the photocurrent density (mA cm^{-2}) obtained using a potentiostat recording the *I-T* curve at 1.23 V versus RHE, λ is the incident light wavelength (nm) from monochromatic, and J_{light} (mW cm^{-2}) is the power density of monochromatic light at a specific wavelength. A source meter (Keithley Instruments Inc., model no. 2400) coupled with the standard Silicon Photodiode (Thorlabs, S120VC) was used to measure the power density of monochromatic light.

PEIS Data: PEIS data were obtained with an alternate current perturbation of 5 mV in amplitude and a 100 mHz to 10⁵ Hz frequency range, both in the dark and under illumination, and under selected direct current potentiostatic conditions (0.30 to 1.60 V vs Ag/AgCl). Nyquist plots (imaginary vs real components of impedance, Z_{Im} vs Z_{Re}) were fitted to the corresponding equivalent circuits via using Z-fit (BioLogic Associates). Fitted capacitances and resistances are calculated based on the electrode geometric area (1 cm²). Error bars were derived from the goodness of the EIS data fittings.

Acknowledgements

Conflict of Interest

The authors declare no conflict of interest.

[1] N. S. Lewis, *Science* **2007**, *315*, 798.

[2] A. Fujishima, K. Honda, *Nature* **1972**, *238*, 37.

[3] A. J. Bard, M. A. Fox, *Acc. Chem. Res.* **1995**, *28*, 141.

[4] K. Sivula, R. V. D. Krol, *Nat. Rev. Mater.* **2016**, *1*, 15010.

[5] V. Andrei, R. L. Z. Hoye, M. Crespo-Quesada, M. Bajada, S. Ahmad, M. D. Volder, R. Friend, E. Reisner, *Adv. Energy Mater.* **2018**, *8*, 1801403.

[6] S. X. Liu, L. X. Zheng, P. P. Yu, S. C. Han, X. S. Fang, *Adv. Funct. Mater.* **2016**, *26*, 3331.

[7] X. Li, S. W. Liu, K. Fan, Z. Q. Liu, B. Song, J. G. Yu, *Adv. Energy Mater.* **2018**, *8*, 1800101.

[8] L. X. Zheng, S. C. Han, H. Liu, P. P. Yu, X. S. Fang, *Small* **2016**, *12*, 1527.

[9] W. X. Ouyang, F. Teng, J. H. He, X. S. Fang, *Adv. Funct. Mater.* **2019**, *29*, 1807672.

[10] N. S. Lewis, *Nat. Nanotechnol.* **2016**, *11*, 1010.

[11] W. Li, S. W. Sheehan, D. He, Y. M. He, X. H. Yao, R. L. Grimm, G. W. Brudvig, D. W. Wang, *Angew. Chem., Int. Ed.* **2015**, *54*, 11428.

[12] J. F. Zhang, R. García-Rodríguez, P. Cameron, S. Eslava, *Energy Environ. Sci.* **2018**, *11*, 2972.

[13] S. Chabi, K. M. Papadantonakis, N. S. Lewis, M. S. Freund, *Energy Environ. Sci.* **2017**, *10*, 1320.

[14] T. Reier, H. N. Nong, D. Teschner, R. Schlögl, P. Strasser, *Adv. Energy Mater.* **2017**, *7*, 1601275.

[15] J. R. McKone, N. S. Lewis, H. B. Gray, *Chem. Mater.* **2014**, *26*, 407.

[16] M. Blasco-Ahicart, J. Soriano-López, J. J. Carbó, J. M. Poblet, J. R. Galan-Mascaros, *Nat. Chem.* **2018**, *10*, 24.

[17] Q. S. Yin, C. L. Hill, *Nat. Chem.* **2018**, *10*, 6.

[18] T. Li, O. Kasian, S. Cherevko, S. Zhang, S. Geiger, C. Scheu, P. Felfer, D. Raabe, B. Gault, K. J. J. Mayrhofer, *Nat. Catal.* **2018**, *1*, 300.

[19] R. Frydendal, E. A. Paoli, I. Chorkendorff, J. Rossmeisl, I. E. L. Stephens, *Adv. Energy Mater.* **2015**, *5*, 1500991.

[20] S. Kumari, B. P. Ajayi, B. Kumar, J. B. Jasinski, M. K. Sunkara, J. M. Spurgeon, *Energy Environ. Sci.* **2017**, *10*, 2432.

[21] I. A. Moreno-Hernandez, C. A. MacFarland, C. G. Read, K. K. Papadantonakis, B. S. Brunschwig, N. S. Lewis, *Energy Environ. Sci.* **2017**, *10*, 2103.

[22] L. L. Zhao, Q. Cao, A. L. Wang, J. Z. Duan, W. J. Zhou, Y. H. Sang, H. Liu, *Nano Energy* **2018**, *45*, 118.

[23] W. L. Kwong, C. C. Lee, A. Shchukarev, E. Björn, J. Messinger, *J. Catal.* **2018**, *365*, 29.

[24] W. L. Kwong, C. C. Lee, A. Shchukarev, J. Messinger, *Chem. Commun.* **2019**, *55*, 5017.

[25] L. J. Han, P. Y. Tang, Á. Reyes-Carmona, B. Rodriguez-Garcia, M. Torrens, J. R. Morante, J. Arbiol, J. R. Galan-Mascaros, *J. Am. Chem. Soc.* **2016**, *138*, 16037.

[26] B. Rodríguez-García, A. Reyes-Carmona, I. Jiménez-Morales, M. Blasco-Ahicart, S. Cavaliere, M. Dupont, D. Jones, J. Rozière, J. R. Galán-Mascarós, F. Jaouen, *Sustainable Energy Fuels* **2018**, *2*, 589.

[27] Y. Y. Zhao, K. R. Yang, Z. C. Wang, X. X. Yan, S. F. Cao, Y. F. Yei, Q. Dong, X. Z. Zhang, J. E. Thorne, L. Jin, K. L. Materna, A. Trimpalish, H. Y. Bai, S. C. Fakrai, X. Y. Zhong, P. Wang, X. Q. Pang, J. H. Guo, M. Flytzani-Stephanopoulos, G. W. Brudvig, V. S. Batistab, D. W. Wang, *Proc. Natl. Acad. Sci. USA* **2018**, *115*, 2902.

[28] W. Li, D. He, S. W. Sheehan, Y. M. He, J. E. Thorne, X. H. Yao, G. W. Brudvig, D. W. Wang, *Energy Environ. Sci.* **2016**, *9*, 1794.

[29] C. H. Cui, M. Heggen, W. D. Zabka, W. Cui, J. Osterwalder, B. Probst, R. Alberto, *Nat. Commun.* **2017**, *8*, 1341.

[30] K. Sivula, F. L. Formal, M. Grätzel, *ChemSusChem* **2011**, *4*, 432.

[31] K. G. U. Wijayantha, S. Saremi-Yarhamadi, L. M. Peter, *Phys. Chem. Chem. Phys.* **2011**, *13*, 5264.

[32] B. Klahr, S. Gimenez, F. Fabregat-Santiago, T. W. Hamann, J. Bisquert, *J. Am. Chem. Soc.* **2012**, *134*, 4294.

[33] A. J. Bard, A. B. Bocarsly, F. R. F. Fan, E. G. Walton, M. S. Wrighton, *J. Am. Chem. Soc.* **1980**, *102*, 3671.

[34] Y. B. Kuang, T. Yamada, K. Domen, *Joule* **2017**, *1*, 290.

[35] S. Giménez, J. Bisquert, *Photoelectrochemical Solar Fuel Production-From Basic Principles To Advanced Devices, [M]*. Springer, Berlin **2016**.

[36] L. Steier, I. Herraiz-Cardona, S. Gimenez, F. Fabregat-Santiago, J. Bisquert, S. D. Tilley, M. Grätzel, *Adv. Funct. Mater.* **2014**, *24*, 7681.

[37] F. S. Hegner, D. Cardenas-Morcoso, S. Gimenez, N. Lopez, J. R. Galan-Mascaros, *ChemSusChem* **2017**, *10*, 4552.

[38] P. Y. Tang, H. B. Xie, C. Ros, L. J. Han, M. Biset-Peiró, Y. M. He, W. Kramer, A. Perez-Rodriguez, E. Saucedo, J. Galan-Mascaros, T. Andreu, J. R. Morante, J. Arbiol, *Energy Environ. Sci.* **2017**, *10*, 2124.

[39] M. Itoi, T. Jike, D. Nishio-Hamane, S. Udagawa, T. Tsuda, S. Kuwabata, K. Boukheddaden, M. J. Andrus, D. R. Talham, *J. Am. Chem. Soc.* **2015**, *137*, 14686.

[40] Y. H. Zhu, J. Ciston, B. Zheng, X. H. Miao, C. Czarnik, Y. C. Pan, R. Sougrat, Z. P. Lai, C. E. Hsiung, K. X. Yao, I. Pinnau, M. Pan, Y. Han, *Nat. Mater.* **2017**, *16*, 532.

[41] D. L. Zhang, Y. H. Zhu, L. M. Liu, X. R. Ying, C. E. Hsiung, R. Sougrat, K. Li, Y. Han, *Science* **2018**, *359*, 675.

[42] M. Martin-Sabi, J. Soriano-López, R. S. Winter, J. J. Chen, L. Vilà-Nadal, D. L. Long, J. R. Galán-Mascarós, L. Cronin, *Nat. Catal.* **2018**, *1*, 208.

[43] S. Pintado, S. Goberna-Ferron, E. C. Escudero-Adan, J. R. Galan-Mascaros, *J. Am. Chem. Soc.* **2013**, *135*, 13270.

[44] B. Klahr, T. Hamann, *J. Phys. Chem. C* **2014**, *118*, 10393.

[45] O. Zandi, T. W. Hamann, *J. Phys. Chem. Lett.* **2014**, *5*, 1522.

[46] J. Suntivich, K. J. May, H. A. Gasteiger, J. B. Goodenough, S. H. Yang, *Science* **2011**, *334*, 1383.

[47] J. Li, R. Peat, L. Peter, *J. Electroanal. Chem. Interfacial Electrochem.* **1984**, *165*, 41.

[48] O. Zandi, T. W. Hamann, *Nat. Chem.* **2016**, *8*, 778.

[49] B. Iandolo, A. Hellman, *Angew. Chem.* **2014**, *126*, 13622.

[50] M. Sachsenhauser, I. D. Sharp, M. Stutzmann, J. A. Garrido, *J. Phys. Chem. C* **2016**, *120*, 6524.

[51] M. R. Nellist, F. A. L. Laskowski, J. J. Qiu, H. Hajibabaei, K. Sivula, T. W. Hamann, S. W. Boettcher, *Nat. Energy* **2018**, *3*, 46.

[52] N. Yatom, O. Neufeld, M. C. Toroker, *J. Phys. Chem. C* **2015**, *119*, 24789.

[53] N. Yatom, Y. Elbaz, S. Navona, M. C. Toroker, *Phys. Chem. Chem. Phys.* **2017**, *19*, 17278.

[54] D. M. Satoca, M. Bartsch, C. Fabrega, A. Genç, S. Reinhard, T. Andreu, J. Arbiol, M. Niederberger, J. R. Morante, *Energy Environ. Sci.* **2015**, *8*, 3242.

[55] T. L. Villarreal, R. Gómez, M. Neumann-Spallart, N. Alonso-Vante, P. Salvador, *J. Phys. Chem. B* **2004**, *108*, 15172.

[56] B. Klahr, S. Gimenez, F. Fabregat-Santiago, J. Bisquert, T. W. Hamann, *Energy Environ. Sci.* **2012**, *5*, 7626.

[57] K. G. Upul Wijayantha, S. Saremi-Yarahmadi, L. M. Peter, *Phys. Chem. Chem. Phys.* **2011**, *13*, 5264.

[58] E. A. Ponomarev, L. M. Peter, *J. Electroanal. Chem.* **1995**, *397*, 45.

[59] M. Heggen, M. Luysberg, K. Tillmann, *J. Large-Scale Res. Facil.* **2016**, *2*, 42.

[60] J. Barthel, L. Houben, K. Tillmann, *J. Large-Scale Res. Facil.* **2015**, *1*, 34.

[61] M. D. L. Mata, R. Leturcq, S. R. Plissard, C. Rolland, C. Magen, J. Arbiol, P. Caroff, *Nano Lett.* **2016**, *16*, 825.

[62] S. Bernal, F. J. Botana, J. J. Calvino, C. Lopez-Cartes, J. A. Perez-Omil, *Ultramicroscopy* **1998**, *72*, 135.

[63] R. R. Zamani, M. Ibanez, M. Luysberg, N. Garcia-Castello, L. Houben, J. D. Prades, V. Grillo, R. E. Dunin-Borkowski, J. R. Morante, A. Cabot, J. Arbiol, *ACS Nano* **2014**, *8*, 2290.